AIAA JOURNAL
Vol. 38, No. 8, August 2000

Subgrid-Scale Models for Large-Eddy Simulations of Compressible Wall Bounded Flows

E. Lenormand* and P. Sagaut†
ONERA, 92322 Châtillon Cedex, France
L. Ta Phuoc‡
ONERA, 91403 Orsay, France
and
P. Comte§
ONERA, 38041 Grenoble Cedex 9, France

A comparative assessment of six subgrid-scale models is presented in the case of a compressible plane channel flow over isothermal walls, four of which are based on the recent mixed-scale model. A supersonic and a subsonic case in temporal development at Mach 1.5 and 0.5, respectively, are considered for a Reynolds number equal to 3000, with comparison to the direct numerical simulations (DNS) of Coleman et al. (Coleman, G. N., Kim, J., and Moser, R. D., "A Numerical Study of Turbulent Supersonic Isothermal-Wall Channel Flow," *Journal of Fluid Mechanics*, Vol. 305, 1995, pp. 159–183) in the first case, and the incompressible DNS of Kim et al. (Kim, J., Moin, P., and Moser, R., "Turbulence Statistics in Fully Developed Channel Flow at Low Reynolds Number," *Journal of Fluid Mechanics*, Vol. 177, 1987, pp. 133–166) in the second case. For each Mach number, two grids are considered, with about 20 and 5 times less grid points as in the reference DNS, and the results are globally satisfactory, although not excellent. In particular, the wall friction is globally underestimated by about 10%, both in the subsonic and the supersonic cases. Among the models tested are several original combinations, which vanish at the wall without requiring any damping function. They are found to improve significantly upon the statistics, in particular near the wall.

I. Introduction

DIRECT numerical simulation (DNS) of turbulent flows at Reynolds numbers encountered in industrial problems is still almost unaffordable because of the large number of scales to be resolved. During the last decades, considerable progress has been made in the use of large-eddy simulation (LES) of turbulent flows, in particular wall-bounded flows. In the LES approach, it is assumed that, when the grid is suffciently refined, the effect of subgrid-scale (SGS) turbulence on the large scales can be accounted for through models depending only on large-scale quantities, yielding a closed system for these. This system is formally close to the full unsteady Navier–Stokes equations, and can be solved explicitly with the same numerical methods as in DNS.

SGS modeling for incompressible flows has been addressed in a large number of studies and a wide range of applications has been investigated (see Refs. 1 and 2 for a review), with quite satisfactory results. For wall-bounded flows, one of the key issues is the ability of SGS models to vanish at the wall.

For compressible wall-bounded flows, extensive experimental investigations reviewed by Morkovin[3] and Bradshaw[4] showed that, for a Mach number up to 5 and in the absence of massive heat transfer at the wall, small-scale turbulent fluctuations were little affected by compressibility. This statement, often referred to as Morkovin's hypothesis in literature, justifies the straightforward extension of the LES approach to compressible flows, with the so-called variable-density extension of the SGS models developed in the incompressible context. Additional closure problems nevertheless arise, and are still widely open. As a matter of fact, only a few attempts are reported in the literature; let us mention the LES of boundary layers at Mach number M between 0.5 and 5 of Normand and Lesieur[5] and Ducros et al.,[6,7] the LES of subsonic ($M = 0.3$ and 0.7) plane channel flows of Ridder and Beddini,[8] the axisymmetric boundary layers at $M = 4.5$ of El Hady et al.,[9] and the supersonic ramp flows of Comte and David[10] and David.[11]

The motivation of the present work is to assess the variable-density extension of several SGS models developed at ONERA. For this purpose, detailed comparisons of turbulent statistics against recent high-quality DNS data at the largest Reynolds number possible are required. The temporal, i.e., streamwise periodic, cool-wall channel-flow DNS of Coleman et al.[12] and Huang et al.[13] at $M = 1.5$ and $Re = 3000$ have been retained, in particular because of the precision of methods used (spectral Fourier–Legendre space differentiation and third-order time integration). These Mach and Reynolds numbers are based on the parameters of the problem, namely, the channel's half height h, the wall temperature T_w, the bulk, i.e., averaged over the whole domain, velocity $u_b = \langle \rho u \rangle / \rho_b$ and density $\rho_b = \langle \rho \rangle$, which are constants of the problem. Another issue is the ability of the compressible LES treatment to recover incompressible results, despite the decreasing effciency of most compressible numerical schemes for low Mach numbers. Results at $M = 0.5$ (and still $Re = 3000$) will therefore be presented briefly, with tentative comparison with incompressible DNS results of Kim et al.[14] (at $Re = 2790$) and experimental data of Niederschulte et al.[15] (at $Re = 2777$) and Kreplin and Eckelmann[16] (at $Re = 3850$). Another motivation for low Mach number investigations is to evaluate the consequences of possible shortcomings in the closure of the compressible equations, which will be helpful to define future strategies of improvement.

The present paper is organized as follows: Sec. II recalls the governing LES equations and their closure, in the footsteps of Vreman et al.[17] (see also Refs. 18 and 19 for additional details). The six SGS models under investigations are briefly presented in Sec. III, and submitted to a priori tests in Sec. IV. The numerical method used for the LES is described in Sec. V. The results are given in Sec. VI, on two different grids for each Mach number. Their resolutions are near direct in the direction normal to the wall, i.e., with $\min(\Delta_z^+) = 1$, to avoid entering the current debate about filter commutation and boundary conditions. In the homogeneous directions, the two levels of resolutions are $(\Delta_x^+, \Delta_z^+) \sim (30, 15)$ and $\sim (60, 30)$

Received 6 November 1998; revision received 18 May 1999; accepted for publication 24 January 2000.

*Ph.D. Student, 29 av. de la Division Leclerc.
†Senior Scientist, 29 av. de la Division Leclerc.
‡Senior Scientist, B.P. 133; also Directeur de Recherches, LIMSI, Centre National de la Recherche Scientifique.
§Senior Scientist, B.P. 53; also Professor, LEGI/IMG, Centre National de la Recherche Scientifique.

for the fine and coarse grids, respectively. Only the fine grids meet the LES-reliability requirements proposed in Refs. 20 and 21. In all cases, simulations without a SGS diverge in all cases, despite that the numerical code is conservative. (Kinetic energy remains bounded but this does not prevent small-scale gradients from piling up.) Thus, although the eddy-viscosity brought about by the different SGS models turns out to be smaller than the molecular viscosity in all cases, the contribution of these models is nevertheless necessary. The comparisons with respect to the DNS results of Refs. 12 and 14 are performed on the grounds of the different profiles of simple first- and second-order statistics shown in these references, without any attempt to filter the DNS data onto our grids or defalter our LES data. Indeed, this would require the precise knowledge of the effective filter of the present simulations, which we do not have. We are, of course, aware of the bias introduced by the unresolved fluctuations in such straightforward comparisons. In the light of Ref. 22 extended to compressible flows, these comparisons are nevertheless expected to be fully relevant for the first-order statistics, including the mean temperature profiles, whose acceptable prediction in LES is difficult.

II. Mathematical Model

The compressible Navier–Stokes equations for an ideal gas of constant R and specific heat ratio γ, read, once nondimensionalized with ρ_b, u_b, T_w, and h, in the following quasi-conservation form:

$$\frac{\partial \rho}{\partial t} + \frac{\partial}{\partial x_j}(\rho u_j) = 0 \tag{1}$$

$$\frac{\partial}{\partial t}(\rho u_i) + \frac{\partial}{\partial x_j}(\rho u_i u_j) + \frac{\partial p}{\partial x_i} + f_1 \delta_{i1} = \frac{\partial \sigma_{ij}}{\partial x_j} \tag{2}$$

$$\frac{\partial E}{\partial t} + \frac{\partial}{\partial x_j}(E + p)u_j + f_1 u_1 = \frac{\partial}{\partial x_j}\sigma_{ij} u_i - \frac{\partial}{\partial x_j} q_j \tag{3}$$

with the total energy, temperature, molecular viscosity, heat flux, and strain-rate and stress tensors, respectively, defined as

$$E = p/(\gamma - 1) + \tfrac{1}{2}\rho u_j u_j \tag{4}$$

$$T = \gamma M_0^2 (p/\rho) \tag{5}$$

$$\mu(T) = T^{0.7} \tag{6}$$

as in Ref. 23,

$$q_j = -\frac{\mu(T)}{(\gamma - 1) Re\, Pr\, M_0^2} \frac{\partial T}{\partial x_j} \tag{7}$$

$$S_{ij} = \frac{\partial u_i}{\partial x_j} + \frac{\partial u_j}{\partial x_i} - \frac{2}{3}\delta_{ij}\frac{\partial u_k}{\partial x_k} \tag{8}$$

$$\sigma_{ij} = [\mu(T)/Re] S_{ij} \tag{9}$$

Summation is applied over repeated indices. Scalar $f_1(t)$ is a forcing term, detailed in Sec. V.B, that ensures constant mass flow rate. The Reynolds, Mach, and Prandtl numbers are $Re = \rho_b u_b h/\mu(T_w)$, $M_0 = \sqrt{(u_b^2/\gamma R T_w)}$, and $Pr = 0.7$.

The LES equations solved in the present study are obtained out of the preceding system thanks to the procedure proposed by Vreman et al.[17,18] or Vreman.[19] As per usual, the projection onto the grid, of local size Δ (defined more rigorously in Sec. III), is assimilated to a low-pass filter (box filter). It commutes with time and space derivatives, accurately in time and along x and y, and only up to a second order in the direction z (normal to the wall) in the case of a stretched grid. The filtered variables are denoted with an overbar. After filtering, the system is made more legible by the introduction of density-weighted variables $\tilde{\phi} = \overline{\rho\phi}/\bar{\rho}$. The originality of the Vreman's approach is that the filtered system is recast in such a way that only computable quantities arise in the left-hand side. This implies the substitution of the filtered energy equation by the exact transport equation of the computable energy:

$$\hat{E} = \bar{p}/(\gamma - 1) + \tfrac{1}{2}\bar{\rho}\tilde{u}_j\tilde{u}_j \tag{10}$$

In the same way, the computable stress tensor and heat flux are introduced:

$$\hat{\sigma}_{ij} = [\mu(\tilde{T})/Re]\tilde{S}_{ij} \tag{11}$$

$$\hat{q}_j = \frac{-\mu(\tilde{T})}{(\gamma - 1) Re Pr M_0^2}\frac{\partial \tilde{T}}{\partial x_j} \tag{12}$$

The exact filtered system reads

$$\frac{\partial \bar{\rho}}{\partial t} + \frac{\partial \bar{\rho}\tilde{u}_j}{\partial x_j} = 0 \tag{13}$$

$$\frac{\partial \bar{\rho}\tilde{u}_i}{\partial t} + \frac{\partial}{\partial x_j}\bar{\rho}\tilde{u}_i\tilde{u}_j + \frac{\partial \bar{p}}{\partial x_i} - \frac{\partial \hat{\sigma}_{ij}}{\partial x_j} + f_1\delta_{i1} = A_1 + A_2 \tag{14}$$

$$\frac{\partial \hat{E}}{\partial t} + \frac{\partial}{\partial x_j}[(\hat{E} + \bar{p})\tilde{u}_j] - \frac{\partial}{\partial x_j}(\hat{\sigma}_{ij}\tilde{u}_i) + \frac{\partial \hat{q}_j}{\partial x_j} + f_1\tilde{u}_1 = -B_1 - B_2 - B_3 + B_4 + B_5 + B_6 - B_7 \tag{15}$$

$$\tilde{T} = \gamma M_0^2 (\bar{p}/\bar{\rho}) \tag{16}$$

Once the subgrid-stress tensor

$$\tau_{ij} = -\bar{\rho}(\widetilde{u_i u_j} - \tilde{u}_i\tilde{u}_j) \tag{17}$$

is introduced, the subgrid terms A_1, A_2, $B_1 \cdots B_7$ read

$$A_1 = \frac{\partial}{\partial x_j}\tau_{ij}, \qquad A_2 = \frac{\partial}{\partial x_j}(\overline{\sigma_{ij}} - \hat{\sigma}_{ij}) \tag{18}$$

$$B_1 = \frac{1}{\gamma - 1}\frac{\partial}{\partial x_j}(\overline{pu_j} - \bar{p}\tilde{u}_j), \qquad B_2 = p\overline{\frac{\partial u_k}{\partial x_k}} - \bar{p}\frac{\partial \tilde{u}_k}{\partial x_k} \tag{19}$$

$$B_3 = -\frac{\partial}{\partial x_j}(\tau_{kj}\tilde{u}_k), \qquad B_4 = -\tau_{kj}\frac{\partial}{\partial x_j}\tilde{u}_k \tag{20}$$

$$B_5 = \overline{\sigma_{kj}\frac{\partial}{\partial x_j}u_k} - \overline{\sigma_{kj}}\frac{\partial}{\partial x_j}\tilde{u}_k, \qquad B_6 = \frac{\partial}{\partial x_j}(\overline{\sigma_{ij}}\tilde{u}_i - \widehat{\sigma_{ij}}\tilde{u}_i) \tag{21}$$

$$B_7 = \frac{\partial}{\partial x_j}(\overline{q_j} - \hat{q}_j) \tag{22}$$

Terms B_1 and B_2 represent the SGS heat flux and pressure-dilatation, respectively.

III. Closure and SGS Modeling

On the grounds of a priori tests in the case of temporally growing mixing layers of convective Mach numbers M_c up to 1.2, Refs. 18 and 19 suggest that terms A_2, B_6, and B_7 can be neglected and that $B_1 + B_2$ can be modeled as a whole with the aid of a variable-density eddy-diffusivity coefficient ν_t, and a turbulent Prandtl number Pr_t, associated to the gradient of $\tilde{T}$:

$$B_1 + B_2 = -\frac{\partial}{\partial x_j}\left(\frac{\bar{\rho}\nu_t}{(\gamma - 1) Pr_t M_0^2}\frac{\partial \tilde{T}}{\partial x_j}\right) \tag{23}$$

In fact, as kindly pointed out by a referee, the pressure-dilatation term B_2 is usually neglected in LES of compressible flows. Equation (23) thus amounts, in practice, to the modeling of the SGS heat flux B_1 by a gradient-transport model. Surprisingly, even at Reynolds numbers large enough not to affect the dominant instabilities of the flow significantly ($Re = 200$ in Ref. 18), the contribution of the viscous term B_5 is found to be rather large, and explicit modeling of it is recommended. Terms B_3 and B_4 are also found to be important, and it is preferred to parameterize them, with the aid of the model for τ_{ij} required for A_1, rather than to neglect them.

These conclusions are certainly not specific to low-Reynolds-number mixing layers. In particular, they should also apply to

sheared homogeneous turbulence,[24] for which the dominant instabilities because of the shear are only weakly affected by compressibility, in contrast with the Kelvin–Helmholtz-type instabilities in mixing layers. Indeed, these instabilities yield the formation of streamwise vortices analogous to those encountered in turbulent Couette flow and channel flow.

In the present case, the DNS results of Coleman et al.[12] and Huang et al.[13] justify the application of the preceding guidelines to channel flow, all the more as the walls are cool. Indeed, Morkovin's hypothesis is globally verified up to $M_0 = 3$, in the sense that compressiblity effects, although quite visible on the mean quantities, affect turbulent fluctuations little. In particular, turbulent Mach numbers are generally lower than about 0.3. Moreover, the pressure–velocity correlations remain small (even at $M_0 = 3$), which should bolster the approximation [Eq. (23)]. This will, however, be disproved by the a priori tests presented in Sec. IV.

Not all SGS models used in this work are eddy-viscosity models; hybrid models for τ_{ij} combining eddy-viscosity and Bardina-type contributions are also considered. In this case, the Bardina-type contribution (which can yield negative SGS energy and cause numerical instability, depending on the type of filter used and the amount of grid stretching in the z direction) is neglected in the modeling of all SGS terms that arise in the energy equation (15), except, of course, B_3 and B_4, which have to be consistent with A_1. Following Ghosal[25] and Horiuti,[26] Vreman proposed to model the low-Reynolds-number term B_5 in the form

$$B_5 = C_\varepsilon \bar{\rho} \left(\tfrac{1}{2}\tau_{\ell\ell}\right)^{\frac{3}{2}} \Big| \Delta \tag{24}$$

in which the (uncomputable) generalized SGS kinetic energy $\frac{1}{2}\tau_{\ell\ell}$ is evaluated, thanks to the eddy-viscosity ν_t introduced before, as

$$\tfrac{1}{2}\tau_{\ell\ell} = \nu_t^2 \Big| \Delta^2 \tag{25}$$

Assuming that the total amount of SGS energy is independent of time (see Ref. 18 for details), C_ϵ is determined dynamically. This yields

$$C_\epsilon = \frac{\int_\Omega [B_1 + B_2 + B_3 + B_4]\, \mathrm{d}\boldsymbol{x}}{\int_\Omega \left[\bar{\rho}\left(\tfrac{1}{2}\tau_{\ell\ell}\right)^{\frac{3}{2}} \Big/ \Delta\right] \mathrm{d}\boldsymbol{x}} \tag{26}$$

where the quantities $B_1 + B_2$, B_3 and B_4 are evaluated.

In the present paper, the grid stretching is rather large, and Deardorff's determination for Δ, namely, the geometric mean between the mesh sizes in the three directions, requires the correction proposed by Scotti et al.,[27] which reads

$$\Delta = (\Delta x_1 \Delta x_2 \Delta x_3)^{\frac{1}{3}} \cosh \sqrt{\tfrac{4}{27}\left[(\ln a_1)^2 - \ln a_1 \ln a_2 + (\ln a_2)^2\right]} \tag{27}$$

where a_1 and a_2 are the two smallest aspect ratios $\Delta x_i / \Delta x_j$.

A. Mixed-Scale Model

Closure will be completed when a model for the SGS tensor τ_{ij} is chosen. Variable-density eddy-viscosity models, i.e., models that assume proportionality between the deviatoric parts of τ_{ij} and S_{ij}, are considered first. The most classical of these variable-density models, due to Smagorinsky (S) (Ref. 28), reads

$$\nu_t = (C_s \Delta)^2 |S(\tilde{u})| \tag{28}$$

where $|S(\tilde{u})| = \sqrt{[S_{ij}(\tilde{u}) S_{ij}(\tilde{u})/2]}$ (second invariant of S_{ij}). The parameter C_s is theoretically found to be equal to 0.18 for incompressible homogeneous isotropic turbulence. In wall-bounded flows, this value yields a well-known overdissipative behavior. To avoid this, Deardorff[29] proposed to reduce the parameter C_s to 0.1. Furthermore, because of its wide dependence on the large scales, this model does not vanish in laminar shear flows and in the near-wall regions. In this last case, the reduced growth of the small scales of turbulence requires the characteristic length-scale to be reduced accordingly. This can be achieved by correcting the mixing length $l_m = C_s \Delta$ with a van-Driest-type damping function, as proposed by Piomelli[30]:

$$l_m = C_s \Delta \left[1 - \exp(-z^+/a)^3\right]^{\frac{1}{2}} \tag{29}$$

where a is a constant taken equal to 25 and z^+ is the distance from the wall expressed in wall units.

The aforementioned drawbacks of the S model can be alleviated by developing models that depend on both the large and the small scales. Sagaut[31] (see also Ref. 32 for a review) proposed a one-parameter (α) family of models for which the eddy viscosity is given by a nonlinear combination of the second invariant of the shear stress tensor, the characteristic length scale Δ, and the kinetic energy q_c^2 of the highest resolved frequencies:

$$\nu_t = C_m |s|^\alpha \left(q_c^2\right)^{(1-\alpha)/2} \Delta^{(1+\alpha)} \tag{30}$$

This also can be viewed as a nonlinear combination of a S and a mixing-length model. For $\alpha = 0$ and 1, the mixing length and S models are retrieved, respectively. When considering homogeneous isotropic turbulence, and $\alpha = \frac{1}{2}$, the value retained throughout this paper, the parameter $C_m = C_m(\alpha)$ is found equal to 0.06 on the basis of an equilibrium assumption between the dissipation and energy-transfer rates.

Introducing a test filter denoted with a hat ($\hat{\tilde{u}}_i = \tilde{u}_{i-1}/4 + \tilde{u}_i/2 + \tilde{u}_{i+1}/4$) that can be interpreted as a second-order approximation of either a Gaussian filter or a top-hat filter (see Ref. 32 or 33 for a review), q_c^2 is evaluated by

$$q_c^2 = \tfrac{1}{2}(\tilde{u}_k - \hat{\tilde{u}}_k)^2 \tag{31}$$

The variable q_c^2 is an approximate evaluation of the kinetic energy q_{sgs}^2 of the subgrid scales. This can be easily proved in the academic case of an incompressible isotropic turbulence following the Kolmogorov law $E(k) = K_0 \epsilon^{2/3} k^{-5/3}$ from wave number k ranging from zero to infinity, in which K_0 and ϵ denote the Kolmogorov constant and the energy-dissipation rate, respectively. Assuming, for the sake of simplicity, the grid and the test filters to be both sharp in the spectral space, with respective cutoff wave numbers k_c and $k_c' < k_c$, one has

$$q_{\mathrm{sgs}}^2 = \int_{k_c}^{\infty} E(k)\, \mathrm{d}k = \frac{3}{2} K_0 \epsilon^{\frac{2}{3}} k_c^{-\frac{2}{3}} \tag{32}$$

$$q_c^2 = \int_{k_c'}^{k_c} E(k)\, \mathrm{d}k = \frac{2}{3} K_0 \epsilon^{\frac{2}{3}} \left(k_c'^{-\frac{2}{3}} - k_c^{-\frac{2}{3}}\right) = \beta q_{\mathrm{sgs}}^2 \tag{33}$$

with

$$\beta = (k_c'/k_c)^{-\frac{2}{3}} - 1 \tag{34}$$

hence $\beta = 1$ and $q_c^2 = q_{\mathrm{sgs}}^2$ for $k_c' = k_c/2\sqrt{2}$. With nonsharp-spectral filters q_c^2 remains proportional to q_{sgs}^2, the proportionality coefficient depending on the filters' transfer functions. When the flow departs from the preceding idealized case, the dependence on q_c^2 of the mixed-scale (MS) model defined in Eq. (30) is expected to improve its adaptation to the local state of the flow in such away that it vanishes in fully resolved and near-wall regions.

B. Selective Mixed-Scale Model

A structural sensor is introduced in the preceding model to improve the prediction of intermittent phenomena. Such a modification was proposed by David[11] (see also Ref. 2 for a review), who introduced a selective function, going to zero in laminar, two-dimensional, or fully resolved regions, to be multiplied to the eddy-viscosity of a given SGS model. This function is based on the local angular fluctuation of the vorticity. The flow is identified as locally underresolved and turbulent when the local angular fluctuation of the highest resolved frequencies is greater than a given threshold angle θ_0. Because the original function proposed by David is discontinuous, and therefore can introduce some numerical instabilities, a continuous selection function has been proposed by Sagaut and Troff[34] (see also Ref. 32):

$$f_{\theta_0}(\theta) = \begin{cases} 1 & \text{if} \quad \theta \geq \theta_0 \\ \tan^{2n}(\theta/2) / \tan^{2n}(\theta_0/2) & \text{otherwise} \end{cases} \tag{35}$$

where θ is the angle between the local filtered vorticity ($\tilde{\omega}$) and the local averaged filtered vorticity ($\hat{\tilde{\omega}}$). The value of θ_0, corresponding to the observed position of the peak of the density probability function for the angular variation of the local vorticity vector in the case of an isotropic homogeneous turbulence is 20 deg. In the present piece of work, n is set equal to 2. The selective variant of an eddy-viscosity model characterized by its ν_t reads

$$\nu_t^{(s)} = \nu_t f_{\theta_0}(\theta) \tag{36}$$

C. Hybrid Models

Genuinely structural models[34] are considered here: all the components of the SGS tensor τ_{ij} are evaluated directly, without the questionable assumption that its deviatoric part is proportional to that of the resolved strain-rate tensor. In an incompressible context, Bardina et al.[35,36] proposed the following scale similarity model:

$$\tau_{ij} \equiv -(\widetilde{u_i u_j} - \tilde{u}_i \tilde{u}_j) = -(\widehat{\tilde{u}_i \tilde{u}_j} - \hat{\tilde{u}}_i \hat{\tilde{u}}_j) = -L_{ij}^m \tag{37}$$

where the hat ($\hat{\cdot}$) denotes a test filter like the one introduced in Eq. (31). A priori tests performed using DNS data[37] have shown that the scale similarity model correlates well with the SGS stress tensor. Nevertheless, when used for a posteriori tests, this model is underdissipative. This can be remedied by linear combination with an eddy-viscosity model, yielding hybrid models of the form

$$\tau_{ij} = \bar{\rho}\left[\alpha' \nu_t S_{ij} - (1-\alpha') L_{ij}^m\right] \tag{38}$$

We will here restrict ourselves to $\alpha_0 = 1/2$ and consider hybrid similarity Smagorinsky (HSS), hybrid similarity mixed scale (HSMS), and hybrid similarity selective mixed scale (HSSMS) models, with ν_t given by Eqs. (28), (30), and (36), respectively.

IV. A Priori Tests

The preceding closure and models are assessed by means of a priori tests against one snaphot of the DNS results of Coleman et al.[12] at Mach 1.5. These data are filtered on the two grids used for the LES (see Sec. VI, in particular Table 4) by means of the second-order centered finite-difference filter $\hat{\cdot}$ used as a test filter by the MS and hybrid-similarity models.

Table 1 shows the tensor-level correlation coefficients

$$\mathcal{C}_{ij} = \text{Correl}[(\tau_{ij})_{\text{true}}, (\tau_{ij})_{\text{modeled}}] \tag{39}$$

with

$$\text{Correl}[a,b] = \frac{\langle ab\rangle - \langle a\rangle\langle b\rangle}{\sqrt{(\langle a^2\rangle - \langle a\rangle^2)(\langle b^2\rangle - \langle b\rangle^2)}} \tag{40}$$

the averages $\langle\ \rangle$ being performed over the whole computational domain. $(\tau_{ij})_{\text{true}}$ and $(\tau_{ij})_{\text{modeled}}$ denote the subgrid-scale stress tensor evaluated a priori and its modelization, respectively.

As expected from Ref. 36, the mixed models exhibit outstanding levels of correlation on both grids. The selection function decreases

Table 1 A priori correlation coefficients at tensor level ($M_0 = 1.5$)

Coefficient	S	HSS	MS	HSMS	SMS	HSSMS
Coarse mesh						
$\mathcal{C}_{11}$	0.26	0.96	0.22	0.96	−0.002	0.96
$\mathcal{C}_{22}$	0.11	0.90	0.13	0.90	0.06	0.91
$\mathcal{C}_{33}$	−0.02	0.89	0.002	0.89	0.03	0.90
$\mathcal{C}_{12}$	0.27	0.80	0.33	0.82	0.22	0.91
$\mathcal{C}_{13}$	0.16	0.91	0.18	0.90	0.12	0.92
$\mathcal{C}_{23}$	0.05	0.85	0.07	0.84	0.08	0.87
Mean value	0.14	0.89	0.16	0.89	0.08	0.91
Fine mesh						
$\mathcal{C}_{11}$	0.55	0.98	0.50	0.98	0.09	0.98
$\mathcal{C}_{22}$	0.09	0.96	0.11	0.96	0.04	0.96
$\mathcal{C}_{33}$	0.006	0.95	0.03	0.95	0.02	0.95
$\mathcal{C}_{12}$	0.04	0.75	0.08	0.84	0.09	0.95
$\mathcal{C}_{13}$	0.16	0.93	0.18	0.94	0.07	0.96
$\mathcal{C}_{23}$	0.08	0.93	0.11	0.94	0.11	0.95
Mean value	0.15	0.92	0.17	0.93	0.07	0.96

Table 2 A priori correlation coefficients at vector level ($M_0 = 1.5$)

Coefficient	S	HSS	MS	HSMS	SMS	HSSMS
Coarse mesh						
$\mathcal{C}_1$	0.25	0.70	0.31	0.74	0.03	0.89
$\mathcal{C}_2$	0.03	0.84	0.11	0.84	0.12	0.86
$\mathcal{C}_3$	0.02	0.73	0.03	0.72	0.03	0.82
Fine mesh						
$\mathcal{C}_1$	0.24	0.76	0.31	0.86	−0.03	0.95
$\mathcal{C}_2$	0.03	0.91	0.09	0.91	0.11	0.93
$\mathcal{C}_3$	0.02	0.87	0.05	0.89	0.09	0.92

Table 3 A priori correlation coefficients at scalar level ($M_0 = 1.5$)

Coefficient	S	HSS	MS	HSMS	SMS	HSSMS
Coarse mesh						
$\mathcal{C}$	0.25	0.71	0.29	0.75	0.02	0.88
$\mathcal{C}_{(B_1+B_2)}$	0.06	0.06	0.01	0.84	−0.01	0.01
$\mathcal{C}_{B_3}$	0.27	0.71	0.32	0.72	0.02	0.88
$\mathcal{C}_{B_4}$	0.44	0.78	0.52	0.75	0.12	0.95
Fine mesh						
$\mathcal{C}$	0.25	0.78	0.31	0.87	−0.04	0.95
$\mathcal{C}_{(B_1+B_2)}$	0.07	0.07	0.09	0.09	0.008	0.008
$\mathcal{C}_{B_3}$	0.25	0.78	0.32	0.86	−0.04	0.88
$\mathcal{C}_{B_4}$	0.27	0.73	0.35	0.84	0.13	0.95

the correlations given by pure eddy-viscosity models such as the MS model. Conversely, it helps the hybrid models by decreasing the contribution of their eddy-viscosity parts, and the largest correlations are obtained with the hybrid similarity selective mixed-scale (HSSMS) model. These trends are confirmed at vector and scalar levels for the following coefficients (Tables 2 and 3):

$$\begin{aligned}
\mathcal{C}_i &= \text{Correl}\left(\left\{\frac{\partial}{\partial x_j}(\tau_{ij})_{\text{true}}\right\}, \left\{\frac{\partial}{\partial x_j}(\tau_{ij})_{\text{modeled}}\right\}\right)\\
\mathcal{C} &= \text{Correl}\left(\left\{\hat{u}_j \frac{\partial}{\partial x_j}(\tau_{ij})_{\text{true}}\right\}, \left\{\hat{u}_j \frac{\partial}{\partial x_j}(\tau_{ij})_{\text{modeled}}\right\}\right)\\
\mathcal{C}_{B_3} &= \text{Correl}\left(\left\{-\frac{\partial}{\partial x_j}[(\tau_{ij})_{\text{true}}\hat{u}_j]\right\}, \left\{-\frac{\partial}{\partial x_j}[(\tau_{ij})_{\text{modeled}}\hat{u}_j]\right\}\right)\\
\mathcal{C}_{B_4} &= \text{Correl}\left(\left\{-(\tau_{ij})_{\text{true}}\frac{\partial}{\partial x_j}\hat{u}_i\right\}, \left\{-(\tau_{ij})_{\text{modeled}}\frac{\partial}{\partial x_j}\hat{u}_j\right\}\right)
\end{aligned} \tag{41}$$

with summation over repeated indices.

Table 3 also shows

$$\mathcal{C}_{(B_1+B_2)} = \text{Correl}\left(\{(B_1+B_2)_{\text{true}}\}, \left\{-\frac{\partial}{\partial x_j}\left(\frac{\bar{\rho}\nu_t}{(\gamma-1)Pr_t M_0^2}\frac{\partial \tilde{T}}{\partial x_j}\right)\right\}\right) \tag{42}$$

$(B_1+B_2)_{\text{true}}$ being evaluated from Eq. (19) with, as shown, the operators $\bar{\cdot}$ and $\tilde{\cdot}$ corresponding to the Reynolds and Favre filtering, respectively, of the DNS data onto the LES grids by means of filter $\hat{\cdot}$. All models and grids tested yield extremely poor values of $\mathcal{C}_{(B_1+B_2)}$, which clearly indicates that the parameterization defined by Eq. (23) is not physically relevant. Furthermore, the magnitude of term $(B_1+B_2)_{\text{true}}$ was found to be no smaller than about half of $(B_3)_{\text{true}}$, depending on the choice of the norm. (The tests were performed with both L_1 and L_2 norms.)

V. Numerical Method

A. Time Integration and Space Discretization

Time integration is performed using the same explicit low-storage third-order Runge–Kutta scheme as in Ref. 38. This scheme is stable for Courant–Friedrichs–Lewy (CFL) numbers up to 1.5, but we will

keep it here lower than 1 (≈ 0.95 in practice) so that the time filtering because of the use of finite time steps is masked by the space-filtering operation. In practice, an adaptive time stepping procedure based on a linear stability analysis is implemented to enhance the computational efficiency.

Convective terms are treated using a fourth-order centered finite-differences scheme while diffusive terms are treated using second-order centered one. In the wall-normal direction, a Cartesian nonuniform grid in combination with a mapping is used to compute the derivatives in a regular computational space. The Jacobian term is computed with a fourth-order centered finite-differencesscheme. To keep aliasing error as small as possible, the convective terms in the Navier–Stokes equations are discretized in their skew-symmetric form, as recommended by Blaisdell et al.[39] and Kravchenko and Moin.[40]

It was checked that the computed results are independent of the selected CFL number. Because the space discretization is achieved with centered nondissipative schemes, it is known that the main sources of dissipation of resolved kinetic energy are the molecular dissipation and the one associated with the SGS models. All of the computations have been carried once again using a centered second-order accurate scheme for convection (not shown here for the sake of brevity). Comparison of the results show that fourth-order accuracy is enough to allow SGS models to play an important role during the computation, making the results reliable to analyze them. A priori tests, which do not incorporate numerical error, are also used to assess the conclusions. Lastly, grid convergence was not investigated because the present paper is dealing with LES, and that the results are intrinsically grid dependent.

B. Forcing Term

Because of the periodic conditions used for the simulation, homogeneity must be preserved by driving the flow with a uniform body force f_1. Averaging the momentum equation (14) over (xy) planes (operator denoted hereafter $\langle\cdot\rangle_p$), integrating the result in the wall normal direction and using symmetry properties, one obtains the time evolution equation for the mass flow rate $Q(t)$:

$$\frac{\mathrm{d}Q}{\mathrm{d}t} = -(2h)L_y f_1 - \frac{2L_y}{Re}\mu(T_w)\frac{\partial\langle u_1\rangle_p}{\partial z}\bigg|_{-h} \tag{43}$$

where L_y is the span of the channel. This expression does not involve the SGS model, which is assumed to vanish at the walls. An extension to compressible flows of the algorithm proposed by Deschamps[41] is used to update the driving term at each time step: assuming that the driving term f_1^n at time step n is known, f_1^{n+1} is given by

$$f_1^{n+1} = f_1^n + \frac{1}{(2h)L_y}\left[\beta_1(Q^{n+1} - Q) + \beta_2(Q^n - Q)\right] \tag{44}$$

where $Q = (2h)L_z\rho_b u_b$ is the mass flux to be preserved, $Q^n = \langle\rho u\rangle(n\Delta t)$ its determination at time step n, and Q^{n+1} a first-order prediction of it at time $(n+1)\Delta t$, given by

$$Q^{n+1} = Q^n - \Delta t L_y L_z f^n + \frac{2L_y}{Re}\mu\frac{\partial\langle u_1^n\rangle_p}{\partial z}\bigg|_{-h} \tag{45}$$

A stability analysis in the incompressible case shows that the algorithm is most efficient for $\beta_1 = 2$ and $\beta_2 = -0.2$, values that have been retained here.

Consistency with the momentum equation requires a driving term of the form $f_1\tilde{u}_1$ in the energy equation. Experience shows that the computation is stable only if one substitutes $f_1\tilde{u}_1$ with $f_1 u_b$, which has the same effect in the mean.

This algorithm has proved to be very efficient in long time integration. Convergence toward Q is rapidly achieved without long-term drift. The maximal relative error is within 0.1% for all the cases that will be presented in this paper.

C. Boundary and Initial Conditions

Isothermal no-slip boundary conditions are imposed at the walls:

$$T = T_w, \qquad u_k = 0 \qquad \text{for} \qquad k = 1, 2, 3 \tag{46}$$

with T_w chosen as reference temperature. The wall pressure p_w is computed as customary by integration of the pressure derivative that arises in the component normal to the wall of the momentum equation, by means of a noncentered second-order scheme for reasons of conformity with applied codes in body-fitted coordinates. The derivatives parallel to the wall are discretized with the same fourth-order scheme as for the interior points. The density and total energy at the wall read

$$\rho_w = p_w / T_w, \qquad E_w = p_w/(\gamma - 1) \tag{47}$$

It is recalled that periodic conditions are used in the streamwise and spanwise directions.

A laminar Poiseuille flow at uniform density and total temperature is imposed as initial condition, with white noise perturbation of amplitude $0.1\,u_b$ for the three velocity components, the thermodynamic variables being left unperturbed.

VI. Applications

The domain dimensions and resolutions for the four cases presented here are recalled in Table 4. All values expressed in wall units (denoted with a plus superscript) are estimations on the basis of the targeted skin friction Reynolds numbers Re_τ that are 180 and 222 for the subsonic and the supersonic cases, respectively (corresponding to the values reported in the reference data by Kim et al.[14] in the subsonic case and of Coleman et al.[12] and Huang et al.[13] in the supersonic case).

The reference DNS results were obtained in a domain of length $L_x = 4\pi h$, which is roughly twice the streamwise correlation distance ~ 1000 wall units at the Reynolds numbers considered (~ 3000), for both Mach numbers. Indeed, it is shown in Ref. 12 that the streamwise correlation distance only increases slowly with the Mach number. With this value of L_x and the same number of grid points m_z in the direction normal to the walls as in Ref. 12, the computational cost would have been too high to test the six SGS models. It was therefore decided to halve L_x in our calculations. In the least favorable case (supersonic), the streamwise correlations for a separation distance of $2\pi h$ do not exceed 0.1, as can be estimated from Fig. 3 of Ref. 13.

The parameters m_x, m_y, m_z and Δ_x^+, Δ_y^+, Δ_z^+ are the number of grid points and the grid spacing for each direction expressed in wall units. As in Refs. 12–14, our grids are uniform in planes parallel to the walls, with stretching normal to the wall. However, the first gridpoint off the wall is located at $z^+ \approx 1$ for both our grids (which are identical in direction z for a given Mach number). This is larger than in Refs. 12–14, for which spectral methods are used, requiring excessive clustering of the collocation points near the walls. Taking into account the difference in L_x mentioned before, the overall resolution on our coarse grid is 9 and 14 times less than that used in Refs. 12–14.

Table 5 briefly recalls the characteristics of the six SGS models used for each case. Note that, whereas the S constant C_s is lowered from 0.18 to 0.1 (see Sec. III.A), the MS model constant C_m is kept

Table 4 Configuration and mesh characteristics

Parameter	Coleman et at.[12]	Coarse mesh	Fine mesh	Kim et al.[14]	Coarse mesh	Fine mesh
M_0	1.5	1.5	1.5	0	0.5	0.5
Re	3000	3000	3000	2790	3000	3000
Re_τ	222	222	222	180	180	180
L_x/h	4π	2π	2π	4π	2π	2π
L_y/h	$4\pi/3$	$4\pi/3$	$4\pi/3$	2π	$4\pi/3$	$4\pi/3$
L_z/h	2	2	2	2	2	2
m_x	144	21	41	192	21	41
m_y	80	31	61	129	31	61
m_z	119	119	119	160	119	119
Δ_x^+	19	69	35	12	57	30
Δ_y^+	12	31	14	7	25	12
$\min(\Delta_z^+)$	0.1	1	1	0.05	1	1
L_x^+	2790	1395	1395	2260	1130	1130
L_y^+	930	930	930	754	754	754
L_z^+	444	444	444	360	360	360

Table 5 Subgrid-scale model characteristics

Short name	Full name	Symbol	Constant	Selective function	Damping function
S	Smagorinsky	····	$C_s = 0.1$	N	Y
HSS	Hybrid similarity Smagorinsky	- - - -	$C_s = 0.1$	N	Y
MS	Mixed-scale	–·–	$C_m = 0.06$	N	N
HSMS	Hybrid similarity mixed-scale	–··–	$C_m = 0.06$	N	N
SMS	Selective mixed-scale	——	$C_m = 0.06$; $\theta_0 = 20°$	Y	N
HSSMS	Hybrid similarity selective mixed-scale	▲	$C_m = 0.06$; $\theta_0 = 20$	Y	N

Table 6 Mean flow variables: coarse mesh, supersonic case

Parameter	Coleman et al.[12]	S	HSS	MS	HSMS	SMS	HSSMS
τ_w	12.12	11.48	12.96	10.69	11.75	11.77	13.00
Re_τ	222	215	233	207	217	219	233
u^*	0.0545	0.0533	0.0555	0.0514	0.0538	0.0538	0.0558
U_c	1.17	1.19	1.16	1.19	1.17	1.16	1.16
T_c	1.378	1.368	1.428	1.370	1.378	1.376	1.416
ρ_c	0.980	0.981	0.978	0.979	0.981	0.982	0.980
ρ_c/ρ_w	0.723	0.729	0.698	0.727	0.723	0.724	0.703

Table 7 Mean flow variables: fine mesh, supersonic case

Parameter	Coleman et al.[12]	S	HSS	MS	HSMS	SMS	HSSMS
τ_w	12.12	10.60	11.79	10.94	11.15	11.37	12.25
Re_τ	222	208	220	211	214	215	225
u^*	0.0545	0.0510	0.0536	0.0517	0.0522	0.0529	0.0545
U_c	1.16	1.18	1.18	1.18	1.17	1.18	1.17
T_c	1.378	1.379	1.388	1.385	1.387	1.374	1.392
ρ_c	0.980	0.981	0.981	0.980	0.980	0.982	0.981
ρ_c/ρ_w	0.723	0.723	0.717	0.719	0.718	0.725	0.715

equal to its value suggested for homogeneous isotropic turbulence. Furthermore, it is recalled that the S and HSS models (and only these two) are helped by a damping function. The turbulent Prandtl number Pr_t is 0.5 in all cases, which is the value found a priori by Moin et al.[23] at the centerline of an incompressible channel flow with passive scalar transport at $Re \sim 3000$.

All of the statistics presented next have been obtained after statistical convergence. The corresponding sampling time is equal to at least five flow-through-time. From now on, for the sake of clarity, all caret, bar, and tilde symbols associated with the resolved variables are left out, and the $\langle\ \rangle$ operator is redefined as the average over time and x–y planes at given distance to the wall $|z|$. This implies averaging over both sides of the channel.

A. Supersonic Case

The quality of the recovery of Coleman et al. DNS results[12,13] at the wall and the centerline is first evaluated in Tables 6 and 7 for all six SGS models considered.

The relative error on the wall shear stress $\tau_w = \mu(T_w)(\partial\langle u\rangle/\partial z)_w$ ranges between -12% and $+7\%$ on the coarse grid, and between -13% and $+1\%$ on the fine grid. The largest negative values are obtained with the classical S and MS models without improvement as resolution increases. The other models perform better in this respect and this is why they are referred to as improved model.

To a lesser extent, the scatter in the skin-friction velocity $u^* = \sqrt{[(1/Re\rho_w)(\partial u/\partial z)_w]}$ and Reynolds number $Re_\tau = \sqrt{[\rho_w Re\text{-}(\partial\langle u\rangle/\partial z)_w]}$ also comes from errors on the wall density ρ_w, which range between -1% and $+3\%$ on the coarse grid and fall within $\pm 1\%$ on the fine grid. The largest errors are positive and come from

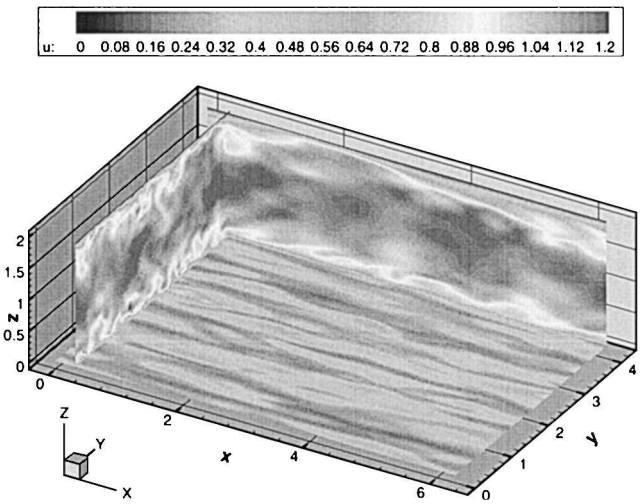

Fig. 1 Isocontours of the instantaneous streamwise velocity component, one of which is about $z^+ = 20$.

the HSS and HSSMS models, especially on the coarse grid, where these models are the only ones that overpredict τ_w. We have no explanation for this counterintuitive behavior. In any case, at this Mach number, τ_w, u^*, and Re_τ show the same trend for a given SGS model. The relative scatter of u^* is within -6% and $+3\%$ on the coarse grid and within -7% and 0% on the fine grid. That of Re_τ is within -7% and $+5\%$ on the coarse grid and within -7% and $+2\%$ on the fine grid. These excursions are quite acceptable considering the state of the art in channel flow LES.

Because the mass-flow rate is correct in all simulations, underprediction of the wall friction yields a slight overestimation of the centerline velocity. The discrepancy does not exceed 3.5%. The same trend is observed on the centerline temperature and, to a lesser extent, on the centerline density, and the ratio ρ_c/ρ_w is almost correct.

Figure 1 shows isocontours of the streamwise velocity fluctuations on three perpendicular planes. The slice parallel to the walls lies at $z^+ \sim 20$. Highly elongated structures are observed, looking very similar to those observed by Coleman et al.,[12] and akin to the streaks found in the incompressible case. In particular, their mean spanwise period is the same: $\lambda^+ = 100$ wall units. The bursting process of the low-speed streaks lifting away from the walls can also be clearly observed. All of these trends demonstrate the overall good behavior of the simulations and are confirmed by the profiles given in Figs. 2 and 3.

The rest of this section is devoted to cross comparisons between SGS models, with particular emphasis on the respective influence of model hybridization and the selection function. Indeed, as can be seen from Tables 6 and 7, no clear-cut grid-independent conclusion can be drawn. Going to higher resolutions to get asymptotic trends would only tell about the capacities of the models at vanishing in fully resolved DNS conditions, which is not the motiviation of the present piece of work. Here, the motivation is to select the best candidates for LES in applied situations, where resolution has to be kept minimal. We will therefore consider with a particular attention the models that yield the least result degradation when going from the fine to the coarse grid. The wall-damped S and the MS models will be considered as classical, and their hybrid and/or selective evolutions referred to as improved models.

Both classical models yield underprediction of the wall friction and overestimation of the centerline velocity on both grids. The MS model slightly benefits from grid refinement, in contrast with the S model that yields the least satisfactory results on the fine grid. Hybridization and selection are both found to be profitable in all cases. The influence of hybridization on the S model is worth noticing, in particular on the coarse grid where, as said before, the HSS model overpredicts the wall friction, as the HSSMS model. On the fine grid, these two models give the best prediction of the wall friction and the centerline velocity.

Let us now look at the mean velocity and temperature profiles. The former (Fig. 2) collapse on the reference data, except for the

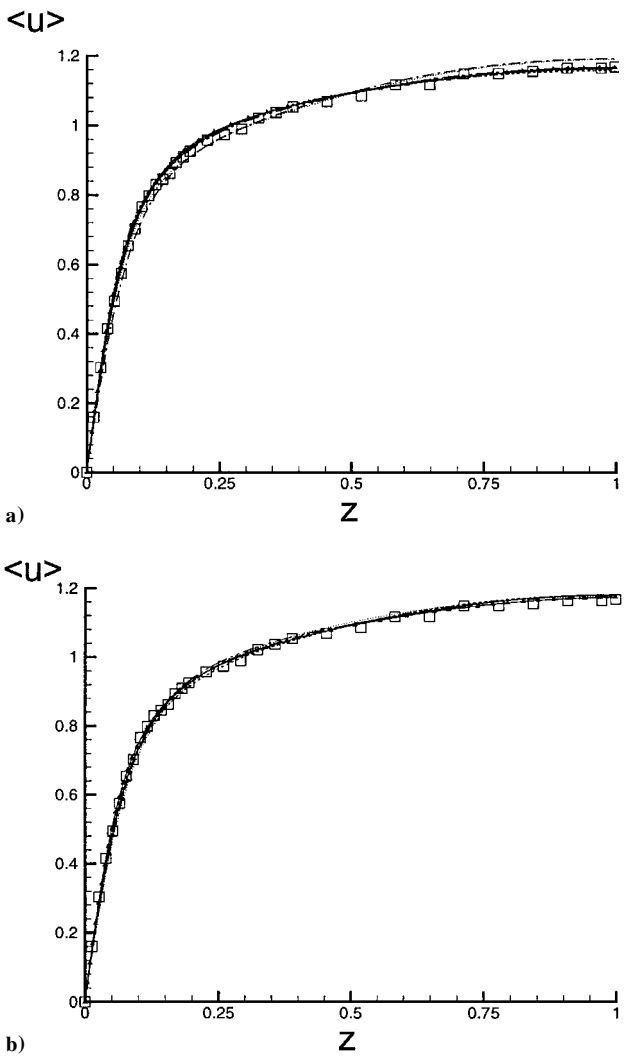

Fig. 2 Mean streamwise velocity profile, $M_0 = 1.5$: a) coarse mesh and b) fine mesh: □, DNS[12]; · · · , S; - - - -, HSS; – –, MS; – · –, HSMS; ——, SMS; and ▲, HSSMS.

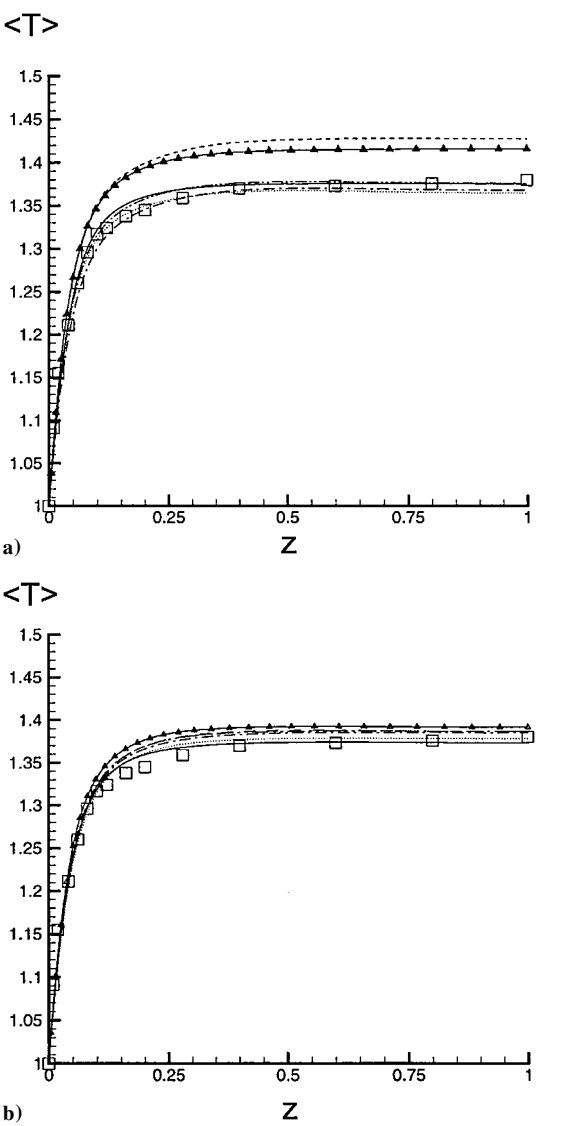

Fig. 3 Mean temperature profile, $M_0 = 1.5$: a) coarse mesh and b) fine mesh: □, DNS[12]; · · · , S; - - - -, HSS; – –, MS; – · –, HSMS; ——, SMS; and ▲, HSSMS.

classical S and MS models on the coarse grid. The latter are more challenging, as can be seen from Fig. 3. The maximum temperature and minimum density are located on the centerline of the channel, the near-wall regions being cooler and denser, because of the isothermal walls. On the fine grid, all temperature profiles collapse on the reference within about 2%. This is also the case on the coarse grid, except for the models that overpredict the wall friction, namely, the HSS and HSSMS models, for which 5% overestimation of the core temperature and wall heat fluxes is observed.

Figure 4 shows that the eddy-viscosity represents between 8% and 37% of the reduced molecular viscosity $1/Re = 33.10^{-5}$ on the fine grid, reaching between 20% and 95% on the coarse grid. This is proof that the coarse grid really challenges the models. Before commenting on the respective behaviors of the models, the following points should be recalled:

1) The constant of the S model is about half the value obtained from infinite-isotropic-Kolmogorov-cascade arguments.

2) The eddy-viscosity of the hybrid models is half that of their nonhybrid counterparts [$(\alpha' = 1/2$ in Eq. (38)].

Although the resulting turbulent fields are different, these points show off on the peak eddy-viscosities, with a ratio $\approx 1/2$ between the MS and the S results on the one hand, and between the S and HSS, the MS and hybrid similarity mixed-scale (HSMS), and the SMS and HSSMS results on the other hand. In comparison, the use of the selection function yields a reduction by about 2/3 of the peak eddy-viscosity on the coarse grid, both between the MS and SMS and betwen the HSMS and HSSMS results. On the fine grid, this reduction factor drops to 1/2 and 1/3, respectively.

The profiles of RMS streamwise velocity fluctuations normalized with the skin friction velocity u^* are shown in Fig. 5, with the distance to the wall expressed in wall units. The classical S and MS models overpredict the peak value, especially on the coarse grid (by up to 30%), which is typical behavior of the state-of-the-art models, as discussed in particular by Najjar and Tafti.[42] The selection function reduces this trend (SMS curves) but does not suppress it. Hybridization seems to be more affective in this respect, but this might be mostly because of the factor $\alpha' = 1/2$ mentioned before. Combination of hybridization and selection (HSSMS model) yields the most satisfactory collapse onto the reference profile (within about 6%) on the coarse grid, but the HSSMS profile falls under it on the fine grid.

Overprediction of the streamwise velocity fluctuations is often associated to underprediction of their wall-normal components w'_{rms}, and this is observed by about 20% in Fig. 6. Surprisingly, the classical S and MS models give the best agreement with the reference on the fine grid, but they suffer more than the improved models from grid coarsening. For w'_{rms}, selection seems to work better than hybridization.

The correlation coefficients of the Reynolds stresses are independent of the Mach number (see, e.g., Ref. 12). Those for $u'w'$ are shown in Fig. 7. The overall agreement with the reference data are rather satisfactory, considering the somewhat disappointing results on w'_{rms} presented. We retrive the fact that classical models behave better on the fine grid, which is not the case for the improved models. Here again, hybridization degrades the results on the fine grid,

Table 8 Mean flow variables: coarse mesh, subsonic case

Parameter	Kim et al.[14]	Dean at $Re = 3000$	S	HSS	MS	HSMS	SMS	HSSMS
τ_w	11.43	12.44	11.13	13.18	10.20	11.84	10.87	13.04
C_f	8.44×10^{-3}	8.29×10^{-3}	7.42×10^{-3}	8.79×10^{-3}	6.80×10^{-3}	7.89×10^{-3}	7.24×10^{-3}	8.70×10^{-3}
Re_τ	180	193	187	203	179	192	185	202
u^*	6.40×10^{-2}	6.44×10^{-2}	5.96×10^{-2}	6.49×10^{-2}	5.71×10^{-2}	6.15×10^{-2}	5.89×10^{-2}	6.46×10^{-2}
U_c	1.16	1.16	1.16	1.14	1.16	1.15	1.15	1.14

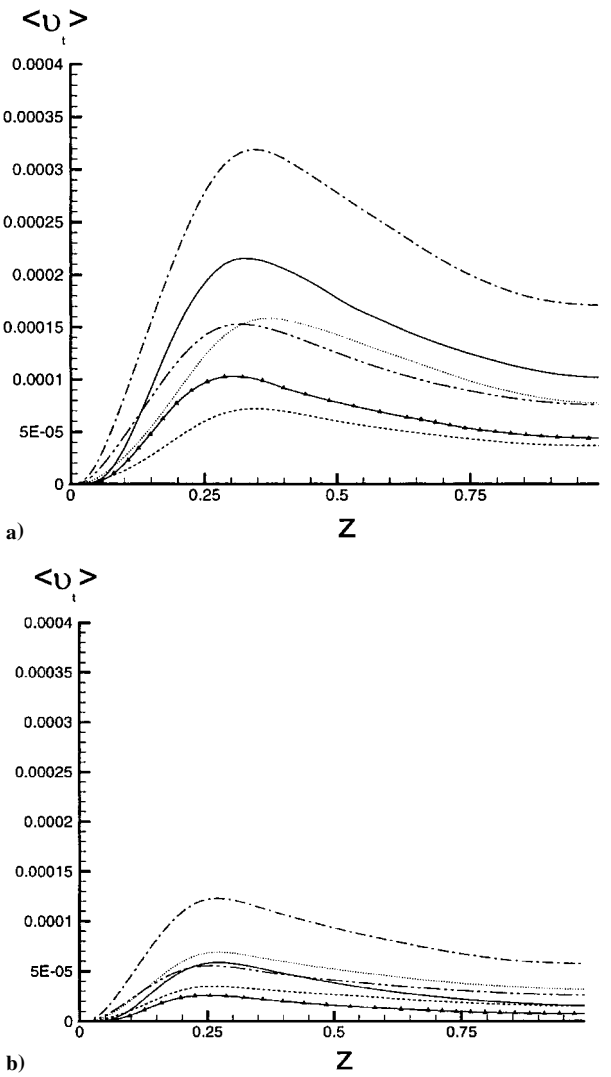

Fig. 4 Eddy viscosity profiles, $M_0 = 1.5$: a) coarse mesh and b) fine mesh: ···, S; ----, HSS; – –, MS; – ·–, HSMS; ——, SMS; and ▲, HSSMS.

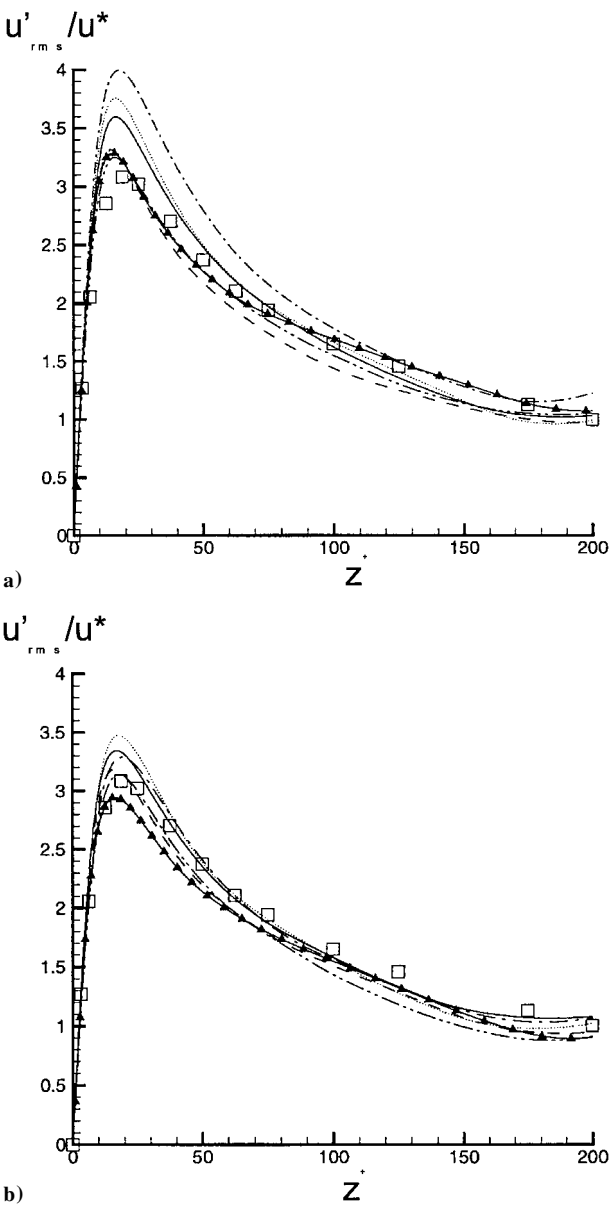

Fig. 5 Streamwise velocity fluctuations normalized by the friction velocity, $M_0 = 1.5$: a) coarse mesh and b) fine mesh: □, DNS[12]; ···, S; ----, HSS; – –, MS; – ·–, HSMS; ——, SMS; and ▲, HSSMS.

in contrast with selection, that acts in a milder way. When combined (HSSMS model), the hybrid behavior usually dominates. For example, on the fine grid, the near-wall overshoot is less overestimated by the HSSMS model than by its nonselective counterpart (HSMS), to the detriment of the core region. At lower resolution, these opposite trends can yield miraculous (but strongly resolution-dependent) compensations.

Let us now look at the fluctuations of the thermodynamical variables. The temperature fluctuations normalized with the mean temperature are shown in Fig. 8. The normalized rms temperature and density fluctuations (not shown here) display the same values, which can be interpreted as a confirmation (if this were necessary) of the Morkovin hypothesis (in short, pressure fluctuations small with respect to the density and temperature fluctuations). On the coarse grid, all SGS models lead to an overestimation of the peak density and temperature fluctuations in the near-wall region. The best prediction of these peak values are obtained with the HSMS model with a relative error of 1%. The largest discrepancies with the reference data are observed using the HSS or the HSSMS models. On the fine grid, the peak value is generally better retrieved, but departures remain rather large away from the wall, which might partly be due to scanning errors on our part (because the centerline derivative of the reference profile does not seem to be zero).

B. Subsonic Case

Tables 8 and 9 summarize the first-order scalar statistics obtained with the different SGS models for the two grids, which differ from those used in the former supersonic case only in the amount of stretching in the z direction, so that the second and penultimate mesh lines are located about $z^+ = 1$ away from the walls in all cases. The

Table 9 Mean flow variables: fine mesh, subsonic case

Parameter	Kim et al.[14]	Dean at Re = 3000	S	HSS	MS	HSMS	SMS	HSSMS
τ_w	11.43	12.44	10.73	12.33	10.71	11.24	11.78	13.06
C_f	8.44×10^{-3}	8.29×10^{-3}	7.15×10^{-3}	8.15×10^{-3}	7.14×10^{-3}	7.49×10^{-3}	7.85×10^{-3}	8.71×10^{-3}
Re_τ	180	193	183	196	183	188	192	202
u^*	6.40×10^{-2}	6.44×10^{-2}	5.85×10^{-2}	6.25×10^{-2}	5.85×10^{-2}	5.99×10^{-2}	6.13×10^{-2}	6.45×10^{-2}
U_c	1.16	1.16	1.17	1.16	1.15	1.16	1.16	1.17

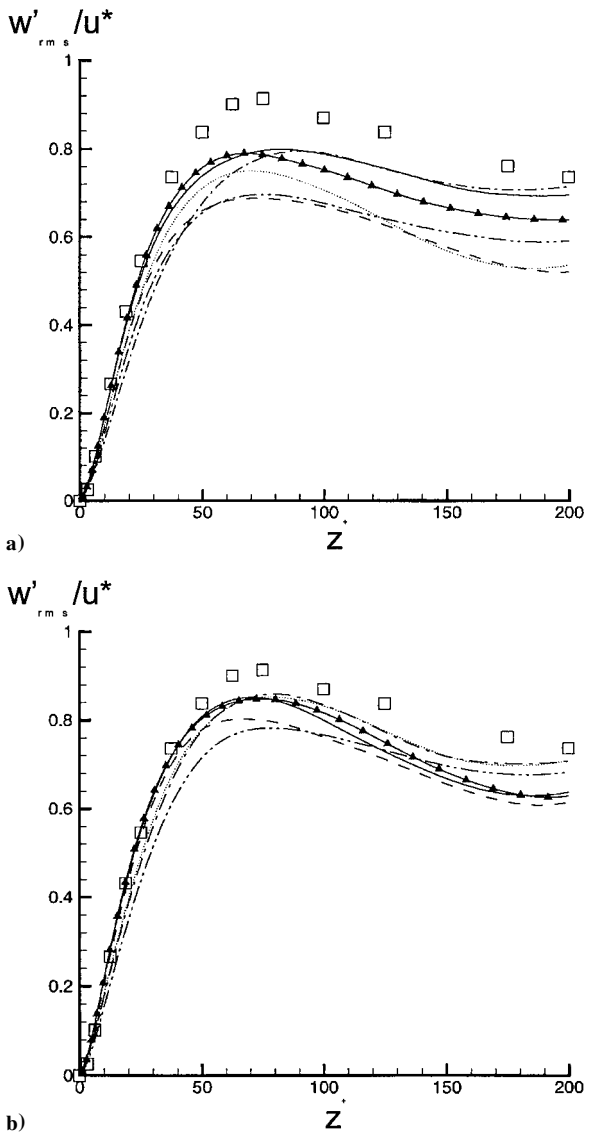

Fig. 6 Wall-normal velocity fluctuations, $M_0 = 1.5$: a) coarse mesh and b) fine mesh: □, DNS[12]; · · · , S; - - - -, HSS; – –, MS; – ·–, HSMS; ——, SMS; and ▲, HSSMS.

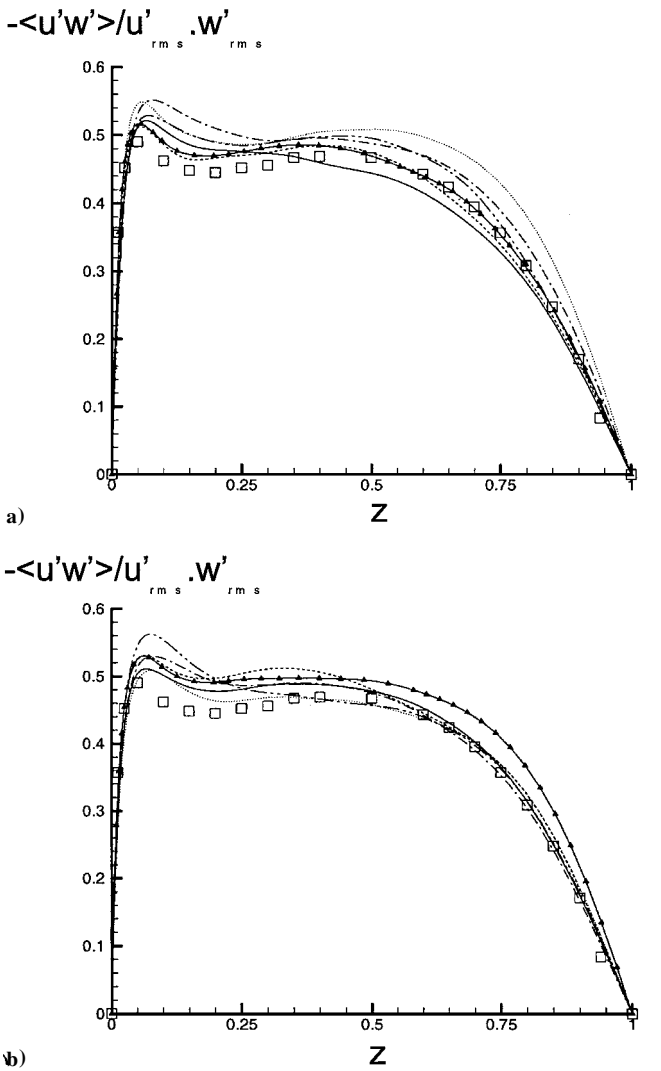

Fig. 7 Correlation coefficients of the Reynolds stress, $M_0 = 1.5$: a) coarse mesh and b) fine mesh: □, DNS[12]; · · · , S; - - - -, HSS; – –, MS; – ·–, HSMS; ——, SMS; and ▲, HSSMS.

same quantities as in Tables 6 and 7 are reported here in addition to the skin friction coefficient $C_f = (2/Re)\tau_w$.

We are unaware of the existence of reliable reference data at $M_0 = 0.5$ and $Re = 3000$. Our turbulent profiles will therefore be compared to the incompressible DNS of Kim et al.[14] and experiments of Niederschulte et al.,[15] for which $Re = 2790$. For the interpretation of the quantities in Tables 8 and 9, we find it more relevant to make use of the Dean correlations

$$U_c = 1.28(2Re)^{-0.0116}, \qquad C_f = 0.073(2Re)^{-0.25} \tag{48}$$

at $Re = 3000$, which appear in the second column of these tables. As expected from the small value of the exponent in Eq. (48), the centerline velocity U_c depends only weakly on the bulk Reynolds number, and this is probably why it is so well retrieved by all of the SGS models under investigation (up to 2% and 1% on the coarse and fine grids, respectively).

The overall relative scatter of τ_w is $[-18\%, +5\%]$ on the coarse grid and $[-14\%, +5\%]$ on the fine grid. That of C_f, Re_τ, and u^* are $[-13\%, +6\%]$, $[-7\%, +5\%]$, and $[-11\%, +3\%]$ on the coarse grid and $[-14\%, -2\%]$, $[-5\%, +5\%]$, and $[-10\%, +0.2\%]$ on the fine grid, respectively. The width of these error bars and the behavior of the different models are about the same as in the supersonic case: drag is generally underestimated, except with models HSS and HSSMS. Note that, on the fine grid, τ_w (hence C_f) and u^* are slightly underpredicted, whereas Re_τ is overpredicted because of a slightly excessive ρ_w.

Detailed comparisons analogous to those in the preceding section have been repeated against the different profiles available in Refs. 14 and 15, yielding globally the same conclusions for all of

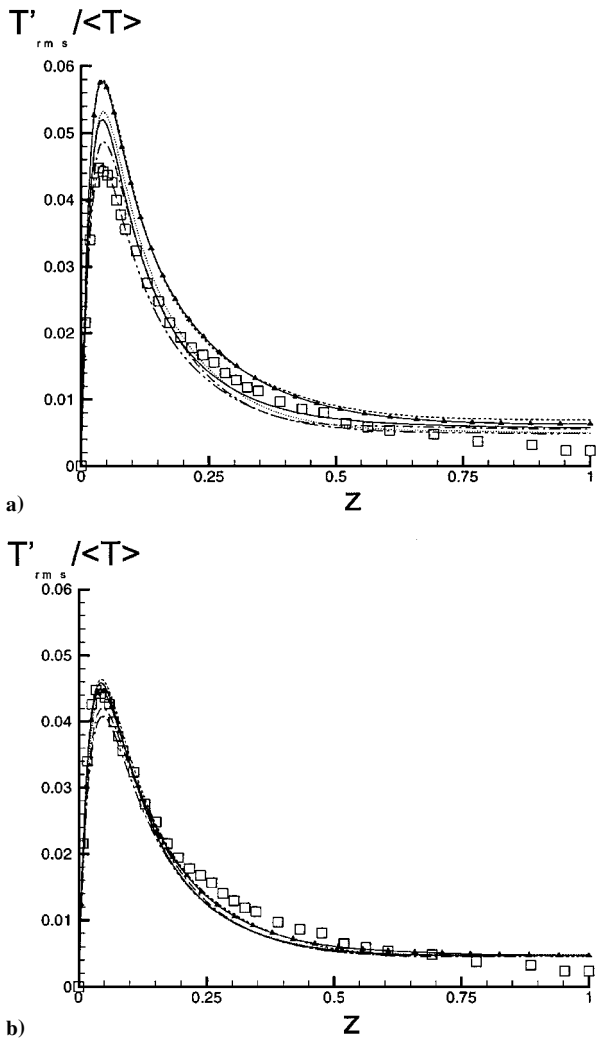

Fig. 8 RMS temperature fluctuations normalized with the mean temperature profile, $M_0 = 1.5$: a) coarse mesh and b) fine mesh: □, DNS[12]; · · ·, S; - - - -, HSS; – –, MS; – ·–, HSMS; ——, SMS; and ▲, HSSMS.

the statistics considered. In particular, the correlation coefficient profiles $-\langle u'w'\rangle/u'w'$ (not shown here for want of room) almost superpose with their counterparts at $M_0 = 1.5$ (Fig. 7), which implies that their Mach number independence is respected by the LES formalism and models considered here.

VII. Conclusions

Large-eddy simulations of wall-bounded compressible flows are performed on a periodic isothermal-wall channel configuration. The convective terms are discretized in their skew-symmetric form using a fourth-order finite-differences scheme, whereas the dissipative terms are discretized by means of a second-order scheme. An original algorithm is proposed for the computation of the forcing term, keeping the flow rate constant within less than 0.1%. Two cases, a supersonic one ($M_0 = 1.5$) and a subsonic one ($M_0 = 0.5$), are considered, with comparison of experimental and DNS results.

With the closure of the equations proposed by Vreman et al., six subgrid-scale models are tested on two different grids for each Mach number to clarify the respective influence of the parameterization and the resolution. Two of the SGS models are based on the S model, whereas the four others are based on a newly proposed MS model, which estimates the subgrid-scale kinetic energy by means of a test filter and scale-similarity arguments. Linear hybridization with a Bardina-type model is also considered, together with the use of a selection function to improve the prediction of intermittent phenomena and alleviate the use of ad hoc damping functions.

A priori tests of the closure and models, performed against the DNS data of Coleman et al.[12] at $M_0 = 1.5$, promote the hybrid models as expected. The selection function is found to decrease the correlations given by pure eddy-viscosity models but yields the opposite effect in the case of hybrid models, by decreasing the contribution of their eddy-viscosity parts. The highest correlation levels (about 0.9 and more) are obtained with the HSSMS model. The eddy-diffusivity closure of the sum of the pressure-velocity and pressure-dilatation terms ($B_1 + B_2$), as proposed by Vreman et al. for free-shear flows, yields extremely poor correlations in the present case, independently of the SGS models and grids used.

Detailed comparisons are made with experimental and DNS data at comparable Reynolds numbers. The overall agreement with these references remains within 20% in all cases, even on the coarse grids for which the average eddy-viscosity is of the same order as the molecular viscosity, the local instantaneous values being much larger, especially those produced by the selective models.

Generally speaking, the MS model gives better results than the wall-damped S model, although it is not helped by ad hoc reduction of its constant. Both are referred to as classical models and underpredict the wall friction, which is found to be the main source of errors. Their hybrid and/or selective counterparts perform better in this respect and deserve being called improved models. The hybridized models (selective or not) can nevertheless yield slight overprediction of the wall friction and the centerline temperature in the supersonic case, especially on coarse grids. In contrast, the SMS model does not exhibit this trend and is less sensitive to grid resolution.

The overall agreement with respect to the experimental and DNS references is about the same for both Mach numbers. This indicates that the lack of theoretical justification of some of the approximations involved in the closure of the energy equation (term $B_1 + B_2$, mostly) and the subsequent counterperformance in a priori tests are not the main source of errors a posteriori. Furthermore, the LES predictions of the quantities reported as independent of the Mach number, e.g., the correlation coefficient of the Reynolds stresses, are found to be so, and the streaky longitudinal structure of the flow is retrieved for both Mach numbers, with average spanwise spacing of about 100 wall units.

Acknowledgments

G. N. Coleman is warmly thanked for having kindly provided the DNS data sets required for the a priori tests. F. Roi is gratefully acknowledged for her contribution to the analysis of the data. This work was supported by the French Ministry of Defence /SPAé.

References

[1]Rogallo, R. S., and Moin, P., "Numerical Simulation of Turbulent Flows," *Annual Review of Fluid Mechanics*, Vol. 16, 1984, pp. 99–137.

[2]Lesieur, M., and Metais, O., "New Trends in Large-Eddy Simulations of Turbulence," *Annual Review of Fluid Mechanics*, Vol. 28, 1996, pp. 45–82.

[3]Morkovin, M. V., "Effects of Compressibility on Turbulent Flows," *Mécanique de la Turbulence*, edited by A. Favre, CNRS Editions, Paris, 1964, pp. 367–380.

[4]Bradshaw, P., "Compressible Turbulent Shear Layers," *Annual Review of Fluid Mechanics*, Vol. 9, 1977, pp. 33–54.

[5]Normand, X., and Lesieur, M., "Direct and Large-Eddy Simulation of Transition in the Compressible Boundary Layer," *Theoretical and Computational Fluid Dynamics*, Vol. 3, No. 3, 1992, pp. 231–252.

[6]Ducros, F., Comte, P., and Lesieur, M., "Large-Eddy Simulation of Transition to Turbulence in a Boundary Layer Developing Spatially over a Flat Plate," *Journal of Fluid Mechanics*, Vol. 326, No. 1, 1996, pp. 1–36.

[7]Ducros, F., Comte, P., and Lesieur, M., "Direct and Large-Eddy Simulations of Transition of a Supersonic Boundary Layer," *Selected Proceedings of Turbulent Shear Flows IX*, edited by F. Durst, N. Kasagi, B. E. Launder, F. W. Schmidt, K. Suzuki, and J. H. Whitelaw, Springer-Verlag, Berlin, 1993, pp. 283–300.

[8]Ridder, J. P., and Beddini, R., "Large-Eddy Simulation of Compressible Channel Flow," NASA TR, Grant NGT-50363, 1993.

[9]El-Hady, N., Zang, T. A., and Piomelli, U., "Application of the Dynamic Subgrid-Scale Model to Axisymmetric Transitional Boundary Layer at High Speed," *Physics of Fluids*, Vol. 6, No. 3, 1994, pp. 1299–1309.

[10]Comte, P., and David, E., "Large-Eddy Simulation of Görtler Vortices in a Curved Compression Ramp," *Proceedings of the Symposium on Experimentation, Modelling and Computation in Flow, Turbulence and Combustion*, edited by J. A. Désidéri, B. N. Chetverushkin, Y. A. Kuznetsov, J. Périaux, and B. Stoufflet, Wiley, New York 1995, pp. 45–61.

[11] David, E., "Modélisation des Écoulements Compressibles et Hypersonics: Une Approche Instationnaire," Doctorat, Inst. National Polytechnique de Grenoble, Grenoble, France, 1993.

[12] Coleman, G. N., Kim, J., and Moser, R. D., "A Numerical Study of Turbulent Supersonic Isothermal-Wall Channel Flow," *Journal of Fluid Mechanics*, Vol. 305, 1995, pp. 159–183.

[13] Huang, P. G., Coleman, G. N., and Bradshaw, P., "Compressible Turbulent Channel Flows: DNS Results and Modelling," *Journal of Fluid Mechanics*, Vol. 305, 1995, pp. 185–218.

[14] Kim, J., Moin, P., and Moser, R., "Turbulence Statistics in Fully Developed Channel Flow at Low Reynolds Number," *Journal of Fluid Mechanics*, Vol. 177, 1987, pp. 133–166.

[15] Niederschulte, M. A., Adrian, R. J., and Hanratty, T. J., "Measurements of Turbulent Flow in a Channel at Low Reynolds Numbers," *Experiments in Fluids*, Vol. 9, No. 4, 1990, pp. 222–230.

[16] Kreplin, H. P., and Eckelmann, H., "Behavior of the Three Fluctuating Velocity Components in the Wall Region of a Turbulent Channel Flow," *Physics of Fluids*, Vol. 22, No. 7, 1979, pp. 1233–1239.

[17] Vreman, B., Geurts, B., and Kuerten, H., "Large-Eddy Simulation of the Turbulent Mixing Layer," *Journal of Fluid Mechanics*, Vol. 339, 1997, pp. 357–390.

[18] Vreman, B., Geurts, B., and Kuerten, H., "A Priori Tests of Large-Eddy Simulation of Compressible Plane Mixing Layer," *Journal of Engineering Mathematics*, Vol. 29, March 1995, pp. 299–327.

[19] Vreman, B., "Direct and Large-Eddy Simulation of the Compressible Turbulent Mixing Layer," Ph.D. Thesis, Univ. of Twente, Twente, The Netherlands, 1995.

[20] Zang, T., "Numerical Simulations of the Dynamics of Turbulent Boundary Layers: Perspectives of a Transition Simulator," *Philosophical Transaction of the Royal Society of London A*, Vol. 336, 1991, pp. 95–102.

[21] Zahrai, S., Bark, F. H., and Karlsson, R. I., "On Anisotropic Subgrid Modelling," *European Journal of Mechanics B/Fluids*, Vol. 14, No. 4, 1995, pp. 459–486.

[22] Härtel, C., and Kleiser, L., "Analysis and Modelling of Subgrid-Scale Motions in Near-Wall Turbulence," *Journal of Fluid Mechanics*, Vol. 356, 1998, pp. 327–352.

[23] Moin, P., Squires, K., Cabot, W., and Lee, S., "A Dynamic Subgrid-Scale Model for Compressible Turbulence and Scalar Transport," *Physics of Fluids A*, Vol. 3, No. 11, 1991, pp. 2746–2757.

[24] Cote, E., Godeferd, F., and Cambon, C., "Effets Structurels de la Compressibilité dans les Écoulements Cisaillés à Grande Vitesse: Amélioration des Modèles Statistiques et de Sousmaille," Ecole Centrale de Lyon, Rapport de synthèse finale, Contrat DRET 95/2585A, Lyon, France, June 1997.

[25] Ghosal, S., "An Analysis of Numerical Errors in Large-Eddy Simulations of Turbulence," *Journal of Computational Physics*, Vol. 125, 1996, pp. 187–206.

[26] Horiuti, K., "Large-Eddy Simulation of Turbulent Channel Flow by One-Equation Modeling," *Journal of the Physical Society of Japan*, Vol. 54, 1985, pp. 2855–2865.

[27] Scotti, A., Meneveau, C., and Lilly, D. K., "Generalized Smagorinsky Model for Anisotropic Grids," *Physics of Fluids A*, Vol. 5, No. 9, 1993, pp. 2306–2308.

[28] Smagorinsky, J., "General Circulation Experiments with the Primitive Equations," *Monthly Weather Review*, Vol. 91, No. 3, 1963, pp. 99–165.

[29] Deardorff, J. W., "A Numerical Study of Three-Dimensional Turbulent Channel Flow at Large Reynolds Number," *Journal of Fluid Mechanics*, Vol. 41, 1970, pp. 453–480.

[30] Piomelli, U., "High Reynolds Number Calculations Using the Dynamic Subgrid-Stress Model," *Physics of Fluids A*, Vol. 5, No. 6, 1993, pp. 1484–1490.

[31] Sagaut, P., "Simulation Numérique d'Écoulements Décollés avec des Modèles de Sous-Maille," Thèse de Doctorat, Université Paris VI, Paris, 1995.

[32] Sagaut, P., *Introduction à la Simulation des Grandes Échelles pour les Écoulements de Fluide Incompressible*, Springer-Verlag, Berlin, 1998.

[33] Sagaut, P., and Grohens, R., "Discrete Filters for Large-Eddy Simulation," *International Journal for Numerical Methods in Fluids*, Vol. 31, Sept. 1999, pp. 1195–1220.

[34] Sagaut, P., and Troff, B., "Subgrid-Scale Model Improvements for Non-Homogeneous Flows," *Advances in DNS/LES*, edited by C. Liu and Z. Liu, Greyden, New York, 1997, pp. 401–408.

[35] Bardina, J., Ferziger, J. H., and Reynolds, W. C., "Improved Turbulence Models Based on Large-Eddy Simulation of Homogeneous, Incompressible, Turbulent Flows," Thermosciences Div., Rept. TF-19, Dept. of Mechanical Engineering, Stanford Univ., Stanford, CA, 1983.

[36] Bardina, J., Ferziger, J. H., and Reynolds, W. C., "Improved Subgrid Scale Models for Large-Eddy Simulation," AIAA Paper 80-1357, 1980.

[37] Horiuti, K., "The Role of the Bardina Model in Large-Eddy Simulation of Turbulent Channel Flow," *Physics of Fluids A*, Vol. 1, No. 2, 1989, pp. 1708–1710.

[38] Lowery, P. S., and Reynolds, W. C., "Numerical Simulation of a Spatially-Developing, Forced, Plane Mixing Layer," Thermosciences Div., Rept. TF-26, Dept. of Mechanical Engineering, Stanford Univ., Stanford, CA, 1986.

[39] Blaisdell, G. A., Spyropoulos, E. T., and Qin, J. H., "The Effect of the Formulation of Nonlinear Terms on Aliasing Errors on Spectral Methods," *Applied Numerical Mathematics*, Vol. 21, No. 2, 1996, pp. 207–219.

[40] Kravchenko, A. G., and Moin, P., "On the Effect of Numerical Errors in Large-Eddy Simulations of Turbulent Flows," *Journal Computational Physics*, Vol. 131, 1997, pp. 310–322.

[41] Deschamps, V., "Simulation Numérique de la Turbulence Inhomogéne Incompressible dans un Écoulement de Canal Plan," ONERA, TR 1988-5, Châtillon, France, 1988.

[42] Najjar, F. M., and Tafti, D. K., "Study of Discrete Test Filters and Finite-Difference Approximations for the Dynamic Subgrid-Scale Stress Model," *Physics of Fluids*, Vol. 8, No. 4, 1996, pp. 1076–1088.

P. Givi
Associate Editor